

# Geochemistry of shales from the Upper Miocene Samh Formation, north Marsa Alam, Red Sea, Egypt: implications for source area weathering, provenance, and tectonic setting

Samir M. Zaid<sup>1</sup>

Received: 22 October 2015 / Accepted: 1 August 2016 / Published online: 12 August 2016  
© Saudi Society for Geosciences 2016

**Abstract** The Upper Miocene shales of the Samh Formation, North Marsa Alam along the Egyptian Red Sea coastal plain were analyzed for major and selected trace elements to infer their provenance, weathering intensity, and tectonic setting. The Samh Formation consists of sandstone underlies by shale and marl intercalations. The Samh shales are texturally classified as mudstones. Mineralogically, these shales consist mainly of smectite and kaolinite, associated with non clay minerals (abundant quartz and trace of plagioclase, microcline, and halite). Compared to post-Archaean Australian shales (PAAS), the Samh shales are highly enriched in SiO<sub>2</sub>, Al<sub>2</sub>O<sub>3</sub>, and Fe<sub>2</sub>O<sub>3</sub> and depleted in TiO<sub>2</sub>, P<sub>2</sub>O<sub>5</sub>, Na<sub>2</sub>O, MgO, and K<sub>2</sub>O contents. The K<sub>2</sub>O/Al<sub>2</sub>O<sub>3</sub> ratio values indicate predominance of clay minerals over K-bearing minerals. Trace elements like zirconium (Zr), Cr, Pb, Sc, Rb, and Cs are positively correlated with Al<sub>2</sub>O<sub>3</sub> indicating that these elements are likely fixed in K-feldspars and clays. The Chemical Index of Alteration (CIA), Plagioclase Index of Alteration (PIA), and Chemical Index of Weathering (CIW) values indicate moderate to intense weathering of the source material in a semiarid climate. The geochemistry results suggest that the Samh shales were deposited in a passive margin of a synrift basin and derived from felsic (granitic) source rocks. The inferred tectonic setting for the Upper Miocene Samh shales in Marsa Alam is in agreement with the tectonic evolutionary history of the Eastern Desert of Egypt during the Upper Miocene.

**Keywords** Provenance · Samh shales · Red Sea · Egypt

✉ Samir M. Zaid  
samir\_zaid75@yahoo.com

<sup>1</sup> Geology Department, Faculty of Sciences, Zagazig University, Zagazig 44511, Egypt

## Introduction

The geochemical composition of clastic sediments is a complex function of variables such as source material, weathering, physical sorting, and diagenesis (Armstrong-Altrin et al. 2004; Moosavirad et al. 2012; Zaid 2013, 2015). Among the terrigenous sedimentary rocks, shales are considered to represent the average crustal composition much better than any other siliciclastic rocks to infer provenance (Nagarajan et al. 2007; Lee 2009), since they preserve the original signature of the source rocks and diagenetic history (Mondal et al. 2012; Spalletti et al. 2012). However, many studies have utilized the geochemical composition of shales and successfully inferred the regional tectonic setting, provenance, weathering conditions, and sediment recycling (Roser and Korsch 1988; McLennan et al. 1993; Cullers 1995). Major element geochemistry of sedimentary rocks is more useful in discriminating the tectonic setting (Bhatia 1983; Roser and Korsch 1986). Armstrong-Altrin and Verma (2005) have warned the use of discrimination diagrams for provenance studies using major element geochemistry. The trace elements such as Th, Cr, Sc, Zr, Hf, and particularly TiO<sub>2</sub> and Al<sub>2</sub>O<sub>3</sub> among other major elements are suitable for provenance and tectonic determination studies, due to their relatively low mobility during sedimentary processes (McLennan et al. 1983; Hayashi et al. 1997). Similarly, they differ in concentration in felsic and basic rocks such as Th enriched in felsic rocks and Sc, Cr, and Co enriched in basic rocks relative to felsic rocks (Armstrong-Altrin et al. 2015b).

Significant contributions have been made by several studies in relation to the regional geology, stratigraphy, paleontology, and sedimentology of the Upper Miocene Samh Formation exposed in southwestern and west

central Sinai, as well as in the Gulf of Suez region (Said 1990; Purser and Philobos 1993). In contrast, little is known about the Upper Miocene rocks along the Egyptian Red Sea coastal plain (e.g., El-Akkad and Dardir 1966; Said 1990; Kora and Abdel-Fattah 2000; Zaid 2002; Issawi et al. 2009), and no detailed studies on geochemistry and tectonic setting have been made. The main purpose of this work is to reconstruct the provenance and tectonic setting of shales of the Upper Miocene Samh Formation, using an integrated approach involving modal analysis and bulk rock geochemistry data from two sections (Wadi Mubarak and Wadi Abu Dabbab; Figs. 1 and 2) in North Marsa Alam, Red Sea, Egypt.

### Geological setting

The study area forms a strip extending for about 40 km between Quseir to North Marsa Alam along the Egyptian

Red Sea coastal plain between latitudes  $25^{\circ} 12' - 25^{\circ} 32' N$  and longitudes  $34^{\circ} 30' - 34^{\circ} 50' E$ . This stretch is bordered by the seashore from the east and the high hills of the pre-Cambrian basement rocks from the west (Fig. 1). The plain is covered mainly with Miocene and Pliocene deposits; pre-Miocene rocks are of limited distribution. The strata have a regional eastward dip to the sea with several NW–SE trending faults. Two stratigraphic successions were studied in detail at Wadi Mubarak–Marsa Mubarak and Wadi Abu Dabbab–Marsa Abu Dabbab areas (Fig. 2).

The tertiary sedimentary rocks exposed in the study area are of Middle–Upper Miocene to Pleistocene age. These rocks classified from older to younger into Gebel El Rusas, Abu Dabbab, Samh, Gabir, and Shagra formations. The Upper Miocene Samh Formation was established by El-Akkad and Dardir (1966). It consists mainly of sandstone that underlies by shale and marl intercalations (Fig. 3a). It overlies unconformably Miocene deposits composed of evaporites of the Abu Dabbab Formation and underlies conformably the Gabir Formation (Fig. 3b). In the study area, the Samh

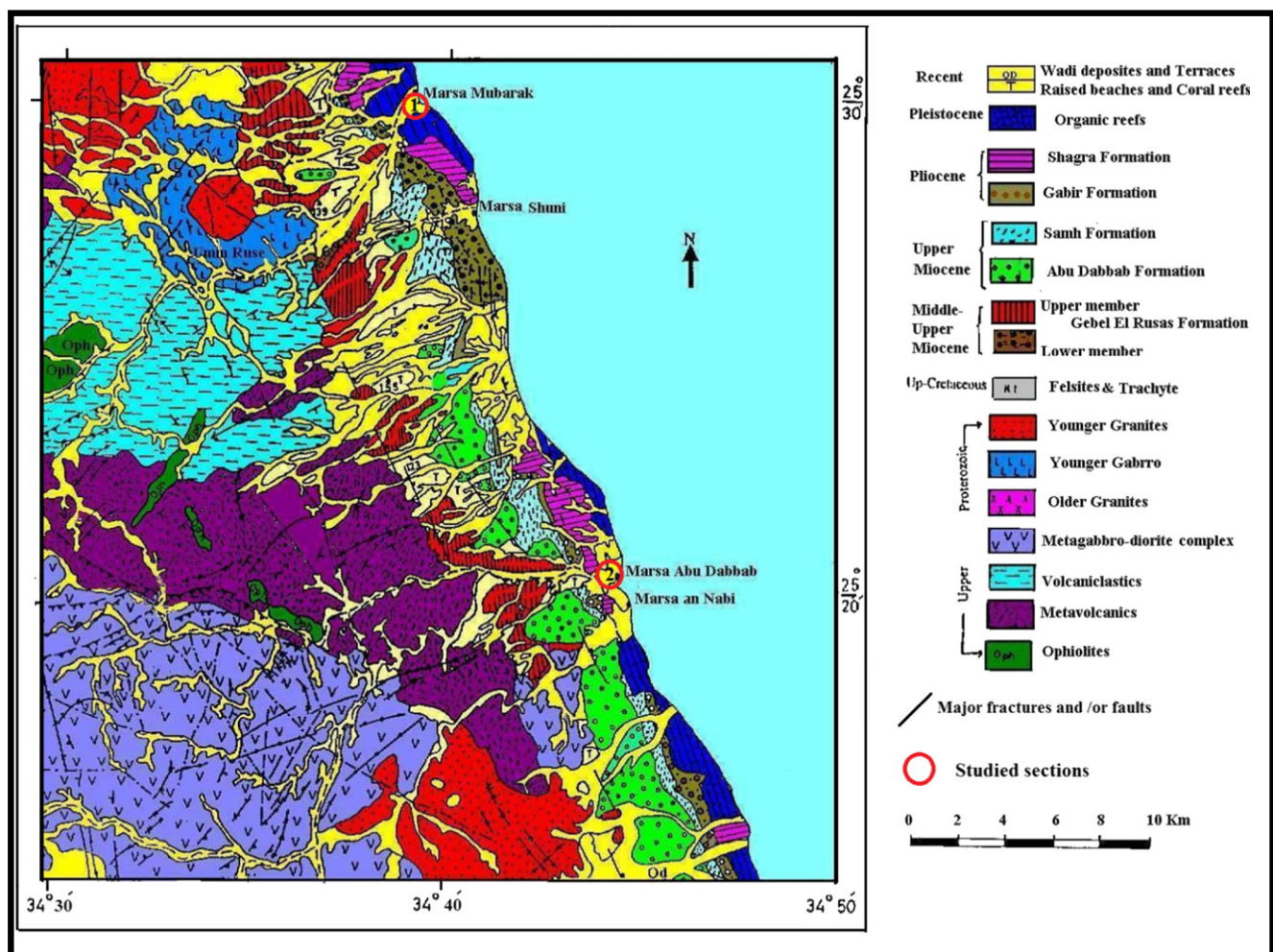


**Fig. 1** Geologic map of North Marsa Alam, showing the location of the study area (modified after Zaid 2002)

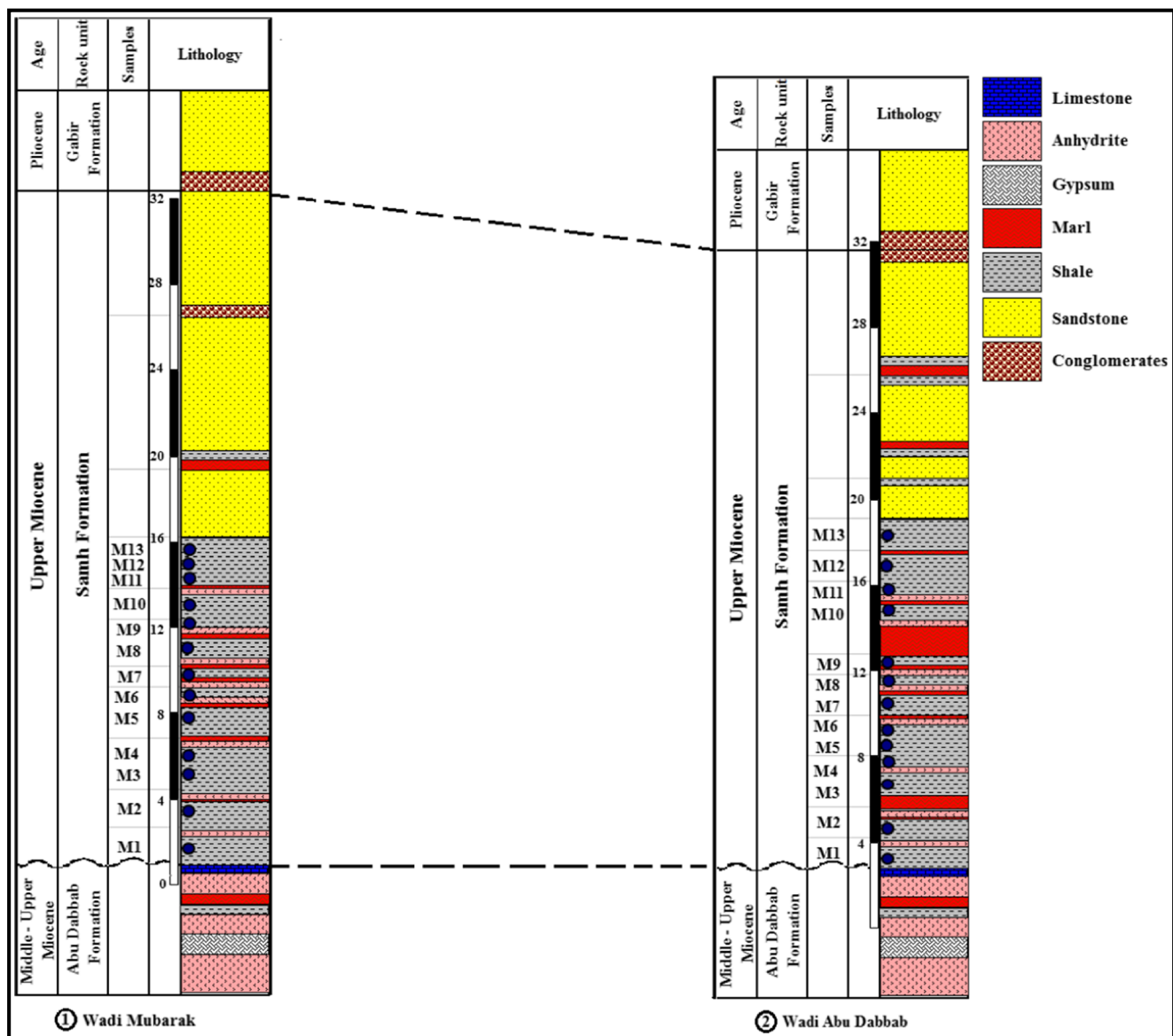


Fig. 2 Correlation chart of the two studied sections, along the Red Sea coast

Formation is easily recognized by its light gray to light green color. Shale is generally soft, fissile with some anhydrite bands (Fig. 3c).

The Upper Miocene Samh Formation forms the slopes of the escarpments (Kora and Abdel-Fattah 2000). With the Samh Formation thinning downward, it measures 32 m thick at Wadi Mubarak and 29 m in thick at Wadi Abu Dabbab. In Wadi Abu Dabbab, the Samh shale is thicker and intercalated by thick beds of marls and contains conglomerate bed at the top (Fig. 2).

A salinity crisis had occurred in the Upper Miocene where a great evaporitic sedimentation took place and resulted in the deposition of the prominent and conspicuous Abu Dabbab Formation. This salinity crisis is attributed partly to a structural uplift resulted in isolation of the Red Sea basin from the parental Mediterranean Sea (Purser and Philobos 1993).

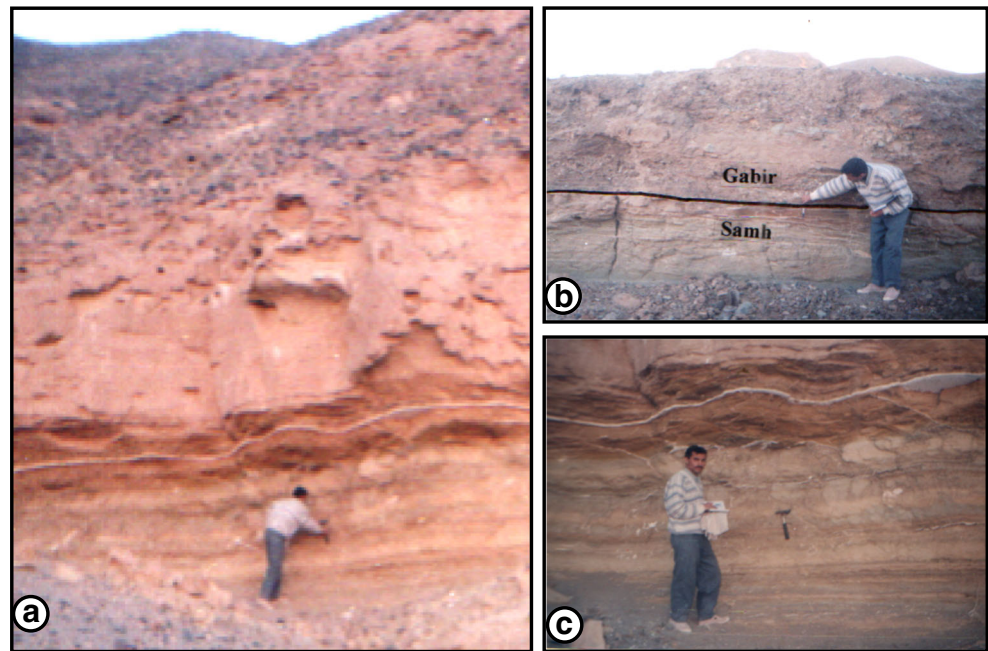
Afterward, before the end of the Miocene, relatively deeper conditions prevailed over the active grabenal area of the Red Sea. This new depositional condition produced fine siliciclastic deposits of the Samh Formation. The composition of the Samh Formation indicates a gradual increase in the depth of the sea from agitated shallow water of shale beds to supratidal at the middle part and becomes intertidal at the upper part (Said 1990; Purser and Philobos 1993; Kora and Abdel-Fattah 2000; Zaid 2002).

### Sampling and methods

Two stratigraphic sections were measured and described representing the Upper Miocene Samh Formation. Twenty-



**Fig. 3** The lithofacies distribution of Samh Formation showing the following: **a** It consists mainly of sandstone underlies by shale and marl intercalation. **b** It underlies conformably the Gabir Formation. **c** Shale is generally soft, light gray to pale green, fissile with some gypsum bands



six representative shale samples were collected from outcrops in Wadi Mubarak and Wadi Abu Dabbab areas (Fig. 2). The petrographic characteristics of six selected samples were investigated by thin section microscopic observations. The mineralogy of 18 shale samples was determined by X-ray diffraction (XRD) analysis using both smear-on glass slide and powder press techniques (Hardy and Tucker 1988). The analysis was done by a Philips X-ray diffractometer model PW/1710 (CuK $\alpha$  radiation with 40 kV, 35 mA, and 2 $^{\circ}$ –70 $^{\circ}$  2-theta). Clay minerals were identified by their characteristic reflections (Moore and Reynolds 1997).

The major oxides and trace elements were determined in 26 bulk samples by X-ray fluorescence spectrometry (XRF), as per the procedure given by Ahmedali (1989). The correlation coefficient has been carried out for the chemical data by using the method of Davis (1986). X-ray fluorescence spectrometry technique and XRD analyses were performed at the laboratories of the National Research Center and Nuclear Materials Authority of Egypt. Analytical precision is better than 5 % for the major oxides and trace elements. Loss on ignition (LOI) was estimated by heating sample at 1000  $^{\circ}$ C for 2 h. Major element data were recalculated to an anhydrous (LOI free) basis and adjusted to 100 % before using them in various diagrams. The total iron is expressed as Fe $_2$ O $_3$ .

## Results

### Mineralogy

The results of the XRD analysis are illustrated in Fig. 4. No obvious qualitative difference is found between the

mineralogical composition of the bulk and the fine (<2  $\mu$ m) fractions of the Upper Miocene Samh shales. The samples are composed mainly of clay minerals (smectite and kaolinite with little illite) associated with non clay minerals (quartz, plagioclase, microcline, and halite). Smectite is the dominant constituent of the clay mineral content of the Upper Miocene Samh shales. The dominance of smectite in Quseir—Marsa Alam is in agreement with the previous results obtained from Hendriks et al. (1990), Ismael (1996), and Ahmed (1997). The origin of smectite was believed by those authors to be due to continental pedogenesis as well as marine neof ormation. Terrestrial smectite in the samples was probably developed under warm to seasonally humid conditions by the degradation of chlorite and illite.

The origin of kaolinite in the shales has been interpreted for a long time as to be a product of chemical weathering and leaching of rocks which occur especially in the exposed granite-metamorphic basement areas in Eastern Desert of Egypt (Gindy 1983). Kaolinite formation is favored under tropical to subtropical humid climatic conditions (Chamley 1989). In addition to a detrital origin, kaolinite may also develop by diagenetic processes due to the circulation of acid solutions (Ghandour et al. 2003). The occurrence of smectite together with kaolinite indicates the alteration of feldspar in connection with an “arenization” (Millot 1970) of crystalline basement rocks in a warm and semiarid climate. Generally, the dominance of smectite in the studied shales at Marsa Alam suggests a terrestrial provenance (Hendriks et al. 1990) that had not attained intensive weathering, a warm and semiarid climate, and the resulted materials were carried by fluvial action, which finally admixed with marine environments.

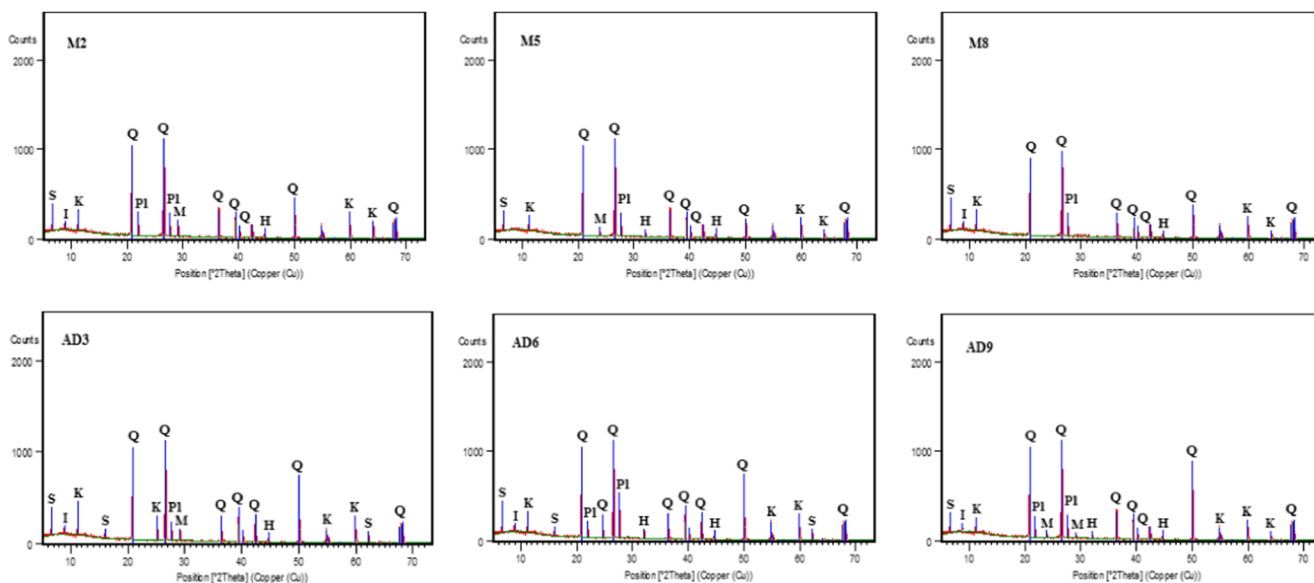


**Fig. 4** X-ray diffractograms of six bulk samples of the Samh shale. *S* smectite, *K* kaolinite, *I* illite, *Q* quartz, *P* plagioclase, *M* microcline, and *H* halite

## Geochemistry

The concentration of major and trace elements of 26 Samh shale samples together with their elemental ratios are reported in Tables 1 and 2. The elemental concentrations of the shales are compared with average shales of Turekian and Wedepohl (1961), Vine and Tourtelot (1970), Gromet et al. (1984) (Table 3). In general, the bulk composition of the Samh shale is comparable with the average shale compositions (Table 3).

### Major element

The shale samples are characterized by the dominance of  $\text{SiO}_2$  (average = 50.3 %). This value closely concurs with the average shales of Turekian and Wedepohl (1961) (58.5; Table 3).  $\text{Al}_2\text{O}_3$  follows  $\text{SiO}_2$  in abundance (average = 13.5 %) which is similar to the average black shales of Vine and Tourtelot (1970) (13.22 %; Table 3). The average content of  $\text{TiO}_2$ ,  $\text{MgO}$ , and  $\text{P}_2\text{O}_5$  in the shales (0.8, 2.8, and 0.1 %, respectively) is nearly similar to that of the North American shale composite of Gromet et al. (1984) (0.8, 2.83, and 0.15 %; Table 3). Also, the average values of  $\text{Na}_2\text{O}$  and  $\text{K}_2\text{O}$  (0.9 and 2.5 %) are similar to the average black shales of Vine and Tourtelot (1970) (0.94 and 2.41 %, respectively). The high content of  $\text{CaO}$  (5.9 %) is considered to be of biochemical origin. The content of  $\text{Fe}_2\text{O}_3$  (3.9 %) is closely similar to the average shale of Turekian and Wedepohl (1961) (4.72 %; Table 3), which indicates the presence of iron oxides and iron minerals.

On the  $\text{Fe}_2\text{O}_3/\text{K}_2\text{O}$  versus  $\text{SiO}_2/\text{Al}_2\text{O}_3$  chemical classification diagram (Fig. 5; Herron 1988), the Samh shales plot in the shale field. The average  $\text{K}_2\text{O}/\text{Na}_2\text{O}$  ratio of the Samh shale varies from 2.27 to 3.31 (average = 2.7); the shale of Wadi Mubarak has lower ratio (average = 2.61) compared to the

shale of Wadi Abu Dabbab (average = 2.82), which is also evidenced from Fig. 6. The ratio is found lower in the Samh shales in comparison to the North American Shale Composite (NASC) and post-Archean Australian Shales (PAAS) (Condie 1993). However,  $\text{SiO}_2/\text{Al}_2\text{O}_3$  ratio among Samh shales shows little variation (average = 3.4–4.22; Table 1).

Figure 7a shows the distribution of major element contents of the shales normalized to PAAS (Taylor and McLennan 1985). Compared to PAAS, the Samh shales are enriched in  $\text{SiO}_2$ ,  $\text{Al}_2\text{O}_3$ , and  $\text{Fe}_2\text{O}_3$  and depleted in  $\text{TiO}_2$ ,  $\text{P}_2\text{O}_5$ , and  $\text{Na}_2\text{O}$  contents and moderately depleted in  $\text{MgO}$  and  $\text{K}_2\text{O}$  contents. Enrichment of  $\text{SiO}_2$ ,  $\text{Al}_2\text{O}_3$ , and  $\text{Fe}_2\text{O}_3$  in Samh shales relative to PAAS indicates the presence of higher quantities of clay minerals and iron oxides. Depletion of  $\text{Na}_2\text{O}$  in the shales relative to PAAS suggests either lesser amount of plagioclase detritus in the shales and/or comparatively intense chemical weathering at the source and during fluvial transportation of the detrital material of the shales (Moosavirad et al. 2011). Depletion of  $\text{TiO}_2$  and  $\text{K}_2\text{O}$  suggests that phyllosilicate minerals exist in lesser quantities in the shales (Condie et al. 1992; Moosavirad et al. 2011). Low contents of  $\text{TiO}_2$  also suggest an evolved (felsic) source rocks.

Major element compositions of the analyzed samples are mainly controlled by clay minerals rather than the nonclay silicate phases. This trend can be illustrated from the values of the index of compositional variation (ICV; Cox et al. 1995) where  $\text{ICV} = (\text{Fe}_2\text{O}_3 + \text{K}_2\text{O} + \text{Na}_2\text{O} + \text{CaO} + \text{MgO} + \text{MnO}) / \text{Al}_2\text{O}_3$ . The trend of ICV values of the Samh shales is wide and varies from 0.68 to 3.29, with an average of 1.3. Values of  $\text{ICV} < 1$  are typical of minerals like kaolinite, illite, and muscovite, and higher values ( $> 1$ ) are characteristic of rock-forming minerals such as plagioclase, K-feldspar, amphiboles, and pyroxenes. In this study, 14 shale samples of the present

**Table 1** Major element concentrations (wt%) of Samh shale

Elements	Wadi Mubarak																Statistical parameters			
	M1	M2	M3	M4	M5	M6	M7	M8	M9	M10	M11	M12	M13	n	Mean	std				
SiO <sub>2adj</sub>	69.12	67.00	66.04	60.75	58.73	63.20	63.37	63.55	63.55	60.86	65.79	63.38	64.33	13	63.82	2.77				
SiO <sub>2</sub>	57.66	56.40	57.06	47.95	44.96	46.95	49.78	49.66	49.88	46.62	54.77	48.80	51.44	13	50.92	4.24				
Al <sub>2</sub> O <sub>3</sub>	14.70	14.88	15.04	12.91	11.43	13.46	14.30	13.98	14.19	12.60	14.38	13.91	14.18	13	13.84	1.02				
CaO	1.48	1.53	1.61	2.82	8.32	2.62	2.62	2.17	2.38	5.46	2.64	2.49	2.40	13	3.11	2.40				
MgO	2.51	2.61	2.81	5.94	2.53	1.91	2.62	2.93	2.40	2.43	2.69	2.18	2.67	13	2.57	0.26				
Fe <sub>2</sub> O <sub>3</sub>	2.26	3.94	5.08	4.98	5.06	5.07	5.14	4.88	5.15	5.04	4.07	5.03	4.70	13	4.65	0.82				
TiO <sub>2</sub>	0.90	0.86	0.84	0.78	0.69	0.84	0.87	0.83	0.81	0.77	0.85	0.85	0.83	13	0.82	0.05				
P <sub>2</sub> O <sub>5</sub>	0.06	0.06	0.08	0.11	0.12	0.08	0.11	0.12	0.10	0.10	0.08	0.08	0.10	13	0.09	0.02				
Na <sub>2</sub> O	1.02	1.01	1.03	0.94	0.91	0.99	0.97	0.99	1.01	0.95	1.00	0.98	1.00	13	0.98	0.03				
K <sub>2</sub> O	2.78	2.84	2.83	2.35	2.33	2.83	2.95	2.45	2.39	2.50	2.70	2.54	2.51	13	2.57	0.20				
SO <sub>3</sub>	0.05	0.05	0.02	0.15	0.20	0.03	0.16	0.13	0.18	0.13	0.07	0.11	0.13	13	0.11	0.06				
LOI	16.52	15.70	13.56	20.55	22.92	25.60	20.92	21.21	20.83	23.22	16.58	22.58	19.54	13	19.98	3.47				
Total	99.94	99.88	99.96	99.48	99.47	99.89	99.47	99.35	99.32	99.82	99.83	99.57	99.50	13	99.65	0.24				
Al <sub>2</sub> O <sub>3</sub> /TiO <sub>2</sub>	16.33	17.30	16.33	16.55	16.57	16.02	16.44	16.84	17.52	16.36	16.92	16.36	17.08	13	16.79	0.54				
SiO <sub>2</sub> /Al <sub>2</sub> O <sub>3</sub>	3.92	3.79	3.79	3.71	3.93	3.49	3.48	3.55	3.52	3.70	3.81	3.51	3.63	13	3.68	0.16				
K <sub>2</sub> O/Na <sub>2</sub> O	2.73	2.81	2.75	2.50	2.56	2.86	2.42	2.47	2.37	2.63	2.70	2.59	2.51	13	2.61	0.15				
K <sub>2</sub> O/Al <sub>2</sub> O <sub>3</sub>	0.19	0.19	0.19	0.18	0.20	0.21	0.16	0.18	0.17	0.20	0.19	0.18	0.18	13	0.19	0.01				
Moles	0.14	0.15	0.15	0.13	0.11	0.13	0.14	0.14	0.14	0.12	0.14	0.14	0.14	13	0.14	0.01				
Al <sub>2</sub> O <sub>3</sub>	0.03	0.03	0.03	0.11	0.15	0.04	0.04	0.04	0.04	0.10	0.05	0.04	0.04	13	0.06	0.04				
CaO*	0.02	0.02	0.02	0.02	0.01	0.02	0.02	0.02	0.02	0.02	0.02	0.02	0.02	13	0.02	0.00				
Na <sub>2</sub> O	0.03	0.03	0.03	0.03	0.03	0.03	0.03	0.03	0.03	0.03	0.03	0.03	0.03	13	0.03	0.00				
K <sub>2</sub> O	0.03	0.03	0.03	0.03	0.03	0.03	0.03	0.03	0.03	0.03	0.03	0.03	0.03	13	0.03	0.00				
CFI	79.35	79.33	79.46	79.17	77.13	77.72	80.97	80.07	80.48	78.03	79.33	79.63	79.96	13	79.28	1.09				
PIA	91.93	92.07	92.02	90.99	89.58	91.18	92.21	91.81	91.81	90.60	91.77	91.78	91.80	13	91.50	0.74				
CIW	93.35	93.48	93.42	92.51	91.52	92.90	93.40	93.15	93.09	92.52	93.21	93.17	93.15	13	92.98	0.56				
ICV	0.68	0.80	0.89	1.32	1.68	0.96	0.93	0.96	0.94	1.30	0.91	0.95	0.94	13	1.02	0.26				

Elements	Wadi Abu Dabbab																Statistical parameters			
	AD1	AD2	AD3	AD4	AD5	AD6	AD7	AD8	AD9	AD10	AD11	AD12	AD13	n	Mean	std				
SiO <sub>2adj</sub>	67.86	65.06	63.06	57.32	68.40	60.47	60.25	51.84	48.96	61.99	63.19	61.33	53.90	13	60.28	5.88				
SiO <sub>2</sub>	57.40	56.88	55.76	50.66	57.66	50.16	48.27	37.74	35.64	52.83	52.20	51.40	40.55	13	49.78	7.40				
Al <sub>2</sub> O <sub>3</sub>	15.04	14.90	13.98	14.05	14.70	14.76	12.88	9.73	8.44	14.50	14.11	13.87	10.35	13	13.18	2.20				
CaO	1.06	4.33	7.23	13.65	3.15	8.29	9.20	13.62	16.40	8.36	6.88	8.24	13.07	13	8.73	4.49				
MgO	2.84	2.66	2.47	2.08	1.58	2.00	3.28	4.90	5.59	1.89	2.29	2.58	4.59	13	2.98	1.26				
Fe <sub>2</sub> O <sub>3</sub>	3.78	3.97	4.15	3.38	2.56	3.29	2.35	3.15	2.94	3.08	2.73	3.26	2.81	13	3.19	0.54				
TiO <sub>2</sub>	0.99	1.10	1.19	0.80	0.66	0.79	0.57	0.76	0.77	0.75	0.67	0.85	0.70	13	0.82	0.18				
P <sub>2</sub> O <sub>5</sub>	0.09	0.09	0.10	0.09	0.05	0.08	0.04	0.11	0.11	0.07	0.06	0.07	0.09	13	0.08	0.02				
Na <sub>2</sub> O	0.78	0.86	0.87	0.81	0.82	0.79	0.92	0.81	0.86	0.81	0.84	0.86	0.86	13	0.84	0.04				
K <sub>2</sub> O	2.58	2.46	2.49	2.38	2.58	2.35	2.49	1.89	1.95	2.44	2.47	2.44	2.11	13	2.36	0.23				
SO <sub>3</sub>	0.03	0.18	0.18	0.48	0.54	0.44	0.11	0.09	0.09	0.49	0.36	0.24	0.10	13	0.26	0.18				
LOI	15.40	12.44	11.40	11.62	15.66	16.93	19.85	26.80	27.10	14.74	17.38	16.06	24.58	13	17.69	5.39				
Total	99.99	99.87	99.82	100	99.96	99.88	99.96	99.60	99.89	99.96	99.99	99.87	99.81	13	99.89	0.11				
Al <sub>2</sub> O <sub>3</sub> /TiO <sub>2</sub>	15.19	13.55	11.75	17.56	22.27	18.68	22.60	12.80	10.96	19.33	21.06	16.32	14.79	13	16.68	3.93				
SiO <sub>2</sub> /Al <sub>2</sub> O <sub>3</sub>	3.82	3.82	3.99	3.61	3.92	3.40	3.75	3.88	4.22	3.64	3.70	3.71	3.92	13	3.80	0.20				
K <sub>2</sub> O/Na <sub>2</sub> O	3.31	2.86	2.86	2.94	3.15	2.97	2.71	2.33	2.27	3.01	2.94	2.84	2.45	13	2.82	0.31				
K <sub>2</sub> O/Al <sub>2</sub> O <sub>3</sub>	0.17	0.17	0.18	0.17	0.18	0.16	0.19	0.19	0.19	0.17	0.18	0.18	0.20	13	0.18	0.02				
Moles	0.15	0.15	0.14	0.14	0.14	0.14	0.13	0.10	0.08	0.14	0.14	0.14	0.10	13	0.13	0.02				
Al <sub>2</sub> O <sub>3</sub>	0.02	0.08	0.13	0.24	0.06	0.15	0.16	0.24	0.29	0.15	0.12	0.15	0.23	13	0.16	0.08				
CaO*	0.01	0.01	0.01	0.01	0.01	0.01	0.01	0.01	0.01	0.01	0.01	0.01	0.01	13	0.01	0.00				
Na <sub>2</sub> O	0.03	0.03	0.03	0.03	0.03	0.03	0.03	0.02	0.02	0.03	0.03	0.03	0.02	13	0.03	0.00				
K <sub>2</sub> O	0.03	0.03	0.03	0.03	0.03	0.03	0.03	0.02	0.02	0.03	0.03	0.03	0.02	13	0.03	0.00				
CFI	81.66	82.93	80.03	80.36	80.96	81.78	78.28	76.78	73.12	81.01	80.43	80.09	76.36	13	79.41	2.58				
PIA	93.97	92.99	92.00	91.72	93.26	92.97	90.55	88.16	84.92	92.63	92.36	91.90	88.29	13	91.21	2.59				
CIW	94.96	94.08	93.33	93.02	94.37	94.02	92.24	90.23	87.98	93.79	93.61	93.23	90.45	13	92.72	2.00				
ICV	0.73	0.96	1.23	1.59	0.73	1.13	1.42	2.50	3.29	1.14	1.08	1.25	2.26	13	1.49	0.76				

Fe<sub>2</sub>O<sub>3</sub>\* total Fe expressed as Fe<sub>2</sub>O<sub>3</sub>; CFI/Al [Al<sub>2</sub>O<sub>3</sub> / (Al<sub>2</sub>O<sub>3</sub> + CaO\* + Na<sub>2</sub>O + K<sub>2</sub>O)] \* 100, Nesbitt and Young 1982; PIA [(Al<sub>2</sub>O<sub>3</sub> - K<sub>2</sub>O) / (Al<sub>2</sub>O<sub>3</sub> + CaO\* + Na<sub>2</sub>O + K<sub>2</sub>O)] \* 100, Fedo et al. 1995; CIW [Al<sub>2</sub>O<sub>3</sub> / (Al<sub>2</sub>O<sub>3</sub> + CaO\* + Na<sub>2</sub>O)] \* 100, Harnois 1988; CaO\* CaO in silicate phase. To calculate CaO\* the assumption proposed by McLemman et al. (1993) was followed; ICI' (Fe<sub>2</sub>O<sub>3</sub> + K<sub>2</sub>O + Na<sub>2</sub>O + CaO + MgO + MnO + TiO<sub>2</sub>) / Al<sub>2</sub>O<sub>3</sub> (Cox et al. 1995)

**Table 2** Trace element concentrations in ppm for shales of the Upper Miocene Samh Formation

Wadi Mubarak														
Elements	M1	M2	M3	M4	M5	M6	M7	M8	M9	M10	M11	M12	M13	Average
Sr	184.0	188.0	178.0	191.0	200.0	170.0	194.0	186.0	193.0	185.3	189.3	184.8	188.8	187.1
Ba	65.0	89.0	37.0	52.0	55.0	45.0	88.0	49.0	48.0	60.8	58.3	47.3	60.0	58.0
V	131.0	137.0	139.0	131.0	133.0	132.0	132.0	130.0	133.0	134.5	135.0	133.8	132.0	133.3
Ni	47.0	53.0	43.0	36.0	41.0	50.0	54.0	49.0	41.0	44.8	43.3	42.5	45.3	45.4
Co	11.0	10.0	11.0	8.5	11.0	9.0	8.0	3.0	12.0	10.1	10.1	9.9	9.1	9.4
Cr	147.0	144.0	147.0	151.0	96.0	90.0	135.0	175.0	166.0	147.3	134.5	121.0	118.0	136.3
Zn	98.0	108.0	97.0	98.0	99.0	96.0	94.0	95.0	91.0	100.3	100.5	97.5	96.8	97.8
Cu	43.0	48.0	46.0	48.0	58.0	56.0	40.0	41.0	53.0	46.1	48.5	51.8	50.3	49.5
Zr	169.0	164.0	167.0	166.0	163.0	171.0	191.0	177.0	183.0	166.5	165.0	166.8	172.8	170.9
Cd	39.0	42.0	1.8	11.0	16.0	17.0	4.0	9.0	6.0	23.5	17.7	11.5	12.0	16.2
U	8.0	9.0	7.0	9.0	9.0	8.5	7.0	6.2	4.1	8.3	8.5	8.4	8.4	7.8
Th	17.0	18.0	19.0	21.0	24.0	19.0	15.0	19.0	21.0	18.8	20.5	20.8	19.8	19.4
Cs	0.5	1.2	0.7	0.8	0.8	0.5	1.0	0.9	0.8	0.8	0.9	0.7	0.8	0.8
Pb	17.0	19.0	20.0	15.0	12.0	18.0	18.0	16.0	19.0	17.8	16.5	16.3	15.8	16.9
Sc	8.8	7.1	7.3	6.8	6.0	7.0	5.9	6.7	6.1	7.5	6.8	6.8	6.4	6.9
Hf	1.1	1.2	0.9	1.1	1.2	1.4	0.90	0.90	0.80	1.1	1.1	1.2	1.2	1.1
Rb	33.5	30.0	32.0	29.0	23.0	31.0	12.0	18.3	21.5	31.1	28.5	28.8	23.8	26.3
Ni/Co	4.3	5.3	3.9	4.2	3.7	5.6	6.8	16.3	3.4	4.4	4.3	4.3	5.0	5.5
Cu/Zn	0.4	0.4	0.5	0.5	0.6	0.6	0.4	0.4	0.6	0.5	0.5	0.5	0.5	0.5
Th/Sc	1.9	2.5	2.6	3.1	4.0	2.7	2.5	2.8	3.4	2.5	3.0	3.1	3.1	2.9
Zr/Sc	19.2	23.1	22.9	24.4	27.2	24.4	32.4	26.4	30.0	22.2	24.3	24.6	26.9	25.2

Wadi Abu Dabbab														
Elements	AD1	AD2	AD3	AD4	AD5	AD6	AD7	AD8	AD9	AD10	AD11	AD12	AD13	Average
Sr	168.0	204.0	208.0	203.0	171.0	199.0	206.0	201.0	203.0	205.0	191.0	195.3	202.7	195.9
Ba	203.0	214.0	252.0	202.0	222.0	241.0	231.0	198.0	187.0	222.7	221.7	229.3	224.7	216.7
V	136.0	145.0	147.0	159.0	173.0	175.0	163.0	147.0	147.0	150.3	169.0	163.5	165.7	154.7
Ni	80.0	66.0	64.0	70.0	60.0	52.0	66.0	64.0	65.0	66.7	60.7	61.5	62.7	65.2
Co	10.0	11.0	12.0	17.0	18.0	11.0	9.0	11.0	9.0	13.3	15.3	14.5	12.3	12.0
Cr	154.0	176.0	164.0	176.0	121.0	124.0	146.0	132.0	90.0	172.0	140.3	146.3	148.7	142.6
Zn	97.0	105.0	103.0	103.0	108.0	102.0	107.0	101.0	120.0	103.7	104.3	104.0	104.0	105.1
Cu	43.0	51.0	58.0	42.0	42.0	45.0	47.0	49.0	40.0	50.3	43.0	46.8	44.7	46.3
Zr	196.0	162.0	184.0	143.0	160.0	208.0	190.0	138.0	135.0	163.0	170.3	173.8	180.3	168.4
Cd	0.9	3.8	4.0	3.0	3.8	3.0	2.8	4.0	6.1	3.6	3.3	3.5	2.9	3.5
U	5.0	4.8	3.5	4.0	3.8	4.0	4.7	4.9	4.8	4.1	3.9	3.8	4.2	4.4
Th	25.0	22.0	19.0	16.0	21.0	23.0	19.0	20.0	20.0	19.0	20.0	19.8	19.3	20.6
Cs	0.8	0.7	0.7	0.6	0.6	0.9	0.7	0.8	0.5	0.7	0.7	0.7	0.7	0.7
Pb	19.0	13.0	9.0	15.0	15.0	11.0	10.0	7.0	8.0	12.3	10.3	10.0	6.0	9.3
Sc	11.0	12.0	11.5	11.0	9.0	11.0	10.0	7.0	7.0	11.5	10.3	10.6	10.7	9.9
Hf	1.11	1.13	1.53	1.53	1.70	1.60	1.70	1.40	1.20	1.4	1.6	1.6	1.6	1.4
Rb	27.0	21.0	21.0	22.0	22.0	21.0	19.0	20.0	20.0	21.3	21.7	21.5	20.7	21.4
Ni/Co	8.0	6.0	5.3	4.1	3.3	4.7	7.3	5.8	7.2	5.0	4.0	4.2	5.1	5.8
Cu/Zn	0.4	0.5	0.6	0.4	0.4	0.4	0.4	0.5	0.3	0.5	0.4	0.4	0.4	0.4
Th/Sc	2.3	1.8	1.7	1.5	2.3	2.1	1.9	2.9	2.9	1.7	1.9	1.9	1.8	2.1
Zr/Sc	17.8	13.5	16.0	13.0	17.8	18.9	19.0	19.7	19.3	14.2	16.5	16.4	16.9	17.2

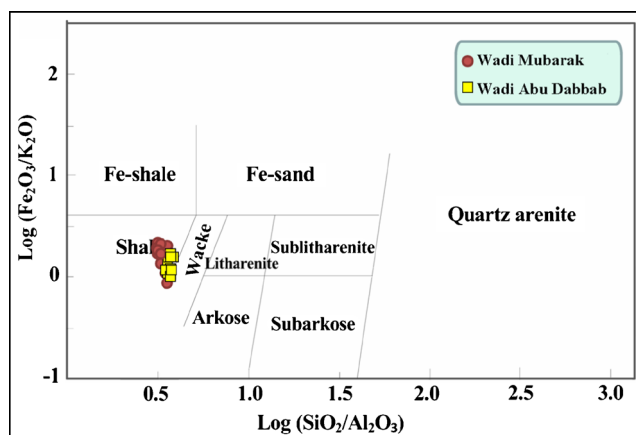
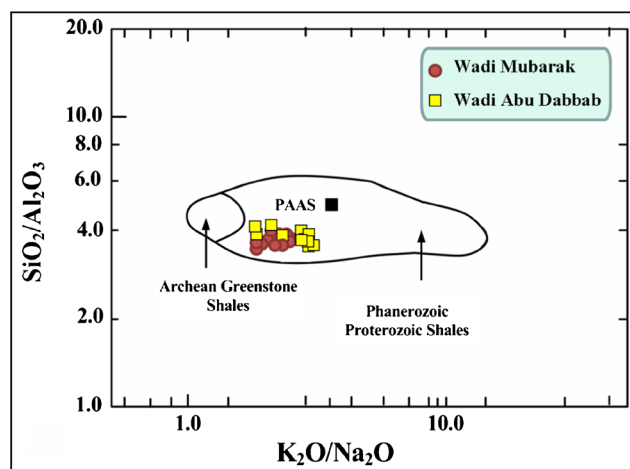


**Table 3** Comparison of chemical composition of the studied shales with published averages

	Present study	1	2	3
SiO <sub>2</sub> %	50.3	64.82	58.50	n.a.
Al <sub>2</sub> O <sub>3</sub> %	13.5	17.05	15.00	13.22
TiO <sub>2</sub> %	0.8	0.80	0.77	0.33
Fe <sub>2</sub> O <sub>3</sub> %	3.9	5.70	4.72	2.86
MgO%	2.8	2.83	2.50	1.77
CaO%	5.9	3.51	3.10	2.10
Na <sub>2</sub> O%	0.9	1.13	1.30	0.94
K <sub>2</sub> O%	2.5	3.97	3.10	2.41
P <sub>2</sub> O <sub>5</sub> %	0.1	0.15	0.16	n.a.
Sr ppm	191.5	142	300	200
Ba ppm	137.3	636	580	300
V ppm	144	130	130	150
Ni ppm	55.3	58	68	50
Cr ppm	139.4	125	90	100
Zn ppm	101.4	n.a.	95	300
Cu ppm	47.4	n.a.	45	70
Zr ppm	169.7	200	160	n.a.

1 NASC (Gromet et al. 1984), 2 average shales (Turekian and Wedepohl 1961), 3 average black shales (Vine and Tourtelot 1970)

study are enriched in clays, and 12 samples are enriched in rock-forming minerals. The values of K<sub>2</sub>O/Al<sub>2</sub>O<sub>3</sub> ratio are different from clay minerals (0.0–0.3) and feldspars (0.3–0.9; Cox et al. 1995). The values of K<sub>2</sub>O/Al<sub>2</sub>O<sub>3</sub> ratio of the Samh shales vary narrowly from 0.16 to 0.23 (average = 0.2). These values also indicate predominance of clay minerals over K-bearing minerals such as K-feldspars and micas (Cox et al. 1995; Moosavirad et al. 2011). The values of Al<sub>2</sub>O<sub>3</sub>/TiO<sub>2</sub> ratio are high (average = 16.7; Table 1) and indicate derivation of the detrital material from a continental source (Fyffe and Pickerill 1993).

**Fig. 5** Geochemical classification diagram using log (SiO<sub>2</sub>/Al<sub>2</sub>O<sub>3</sub>)–log (Fe<sub>2</sub>O<sub>3</sub>/K<sub>2</sub>O) (after Herron 1988)**Fig. 6** SiO<sub>2</sub>/Al<sub>2</sub>O<sub>3</sub> versus K<sub>2</sub>O/Na<sub>2</sub>O bivariate plot

SiO<sub>2</sub> exhibits a strong negative correlation with CaO ( $r = -0.75$ ) and P<sub>2</sub>O<sub>5</sub> ( $r = -0.59$ ,  $n = 26$ ) indicating decrease of calcite and phosphate with increasing contents of quartz. SiO<sub>2</sub> shows statistically significant correlation with Al<sub>2</sub>O<sub>3</sub> ( $r = 0.95$ ), TiO<sub>2</sub> ( $r = 0.50$ ) and K<sub>2</sub>O ( $r = 0.81$ ,  $n = 26$ ). Al<sub>2</sub>O<sub>3</sub> exhibits statistically significant correlation with TiO<sub>2</sub> ( $r = 0.57$ ) and K<sub>2</sub>O ( $r = 0.77$ ,  $n = 26$ ). These linear relationships suggest detrital sorting effect of sediments during transportation. The K<sub>2</sub>O/Na<sub>2</sub>O ratio values (average = 2.7) indicate the presence of K-bearing minerals such as K-feldspar, muscovite, and biotite. Although Na<sub>2</sub>O statistically significant correlation with Fe<sub>2</sub>O<sub>3</sub> ( $r = 0.49$ ,  $n = 26$ ) and negative correlation with CaO, MgO, TiO<sub>2</sub>, and P<sub>2</sub>O<sub>5</sub>, suggest the presence of smectite (Nagarajan et al. 2007).

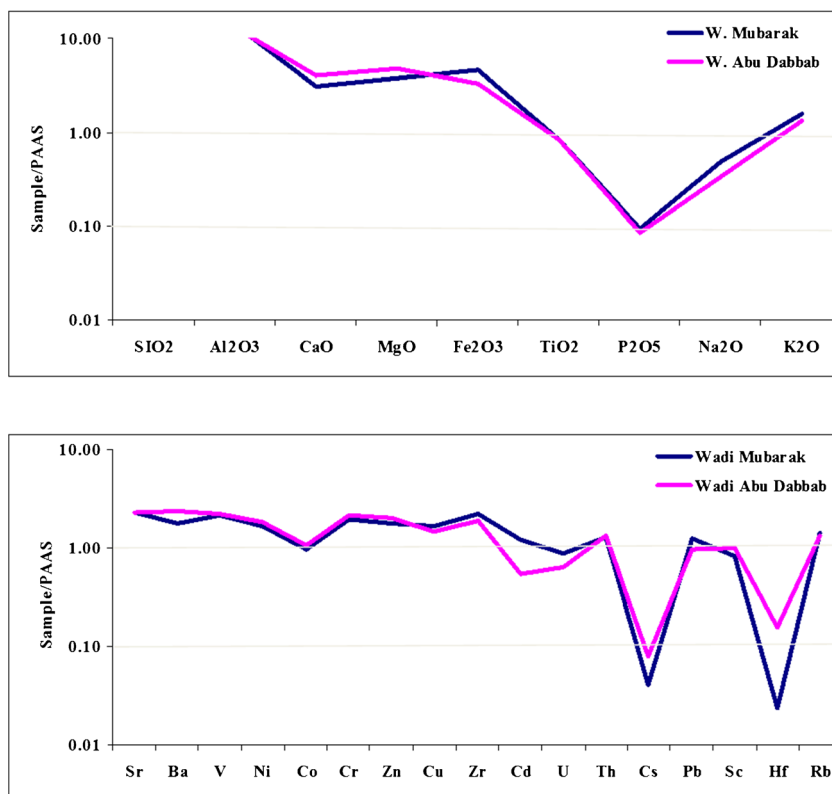
#### Trace element

Zirconium (Zr) shows an average of 169.7 ppm; this value closely concurs with the average shales of Turekian and Wedepohl (1961) and NASC of Gromet et al. (1984) (160 and 200 ppm, respectively). It has an average of 191.5 ppm, which is closely similar to the average black shales of Vine and Tourtelot 1970 (200 ppm), identifying that Sr may be concentrated by noncalcareous plankton (Knauer and Martin 1973), and especially aragonitic materials and shells. The average Ni content (55.3 ppm) is similar to the average shales of NASC of Gromet et al. (1984) (58 ppm) and higher than average black shales of Vine and Tourtelot 1970 (50 ppm). This indicates that Ni may be associated with organic matter. The average Zn and Cu contents in the studied samples is 101.4 and 47.4 ppm, respectively, these values are slightly similar to that average shale (95 and 45 ppm, respectively) of Turekian and Wedepohl (1961).

In comparison to PAAS, the Upper Miocene Samh shales are lower in large ion lithophile trace elements (Rb, Cs, and Ba) and transition trace elements (Co, Ni, Sc, and Cu) (Fig. 7b). Trace elements like Zr, Cr, Pb, Sc, Rb, and Cs are



**Fig. 7** Distribution of PAAS normalized abundance of Samh Shale: **a** major and **b** trace elements



positively correlated with  $\text{Al}_2\text{O}_3$  ( $r = 0.59, 0.54, 0.52, 0.38, 0.26$ , and  $0.25$ , respectively;  $n = 26$ ), indicating that these elements are likely fixed in K-feldspars and clays (Armstrong-Altrin et al. 2015b). On the other hand, the correlation of  $\text{Al}_2\text{O}_3$  versus Co, Cd, V, U, Cu, Ni, Th, Ba, Hf, Sr, and Zn is statistically not significant ( $r = 0.16, 0.12, 0.01, -0.001, -0.06, -0.07, -0.08, -0.09, -0.12, -0.42$ , and  $-0.45$ , respectively;  $n = 26$ ), indicating that they are not likely bound in the clay minerals (Armstrong-Altrin 2009).

## Discussion

### Weathering and sediment recycling

The intensity of chemical weathering is controlled by various factors: source rock composition, climatic conditions, duration of weathering, and rates of tectonic uplift of source region (e.g., Akarish and El-Gohary 2008; Moosavirad et al. 2011). During these processes, the large cations (e.g., Ba and Al) remain preserved in the weathering residue in contrast to the smaller cations (Na, Ca, and Sr) that can be selectively removed (Fedo et al. 1996; Nath et al. 2000; Akarish and El-Gohary 2008). The degree of weathering is quantified by various methods. A few indices of weathering have been proposed based on the abundances of mobile and immobile element oxides ( $\text{Na}_2\text{O}$ , CaO,  $\text{K}_2\text{O}$ , and  $\text{Al}_2\text{O}_3$ ). Among different

indices of weathering, the Chemical Index of Alteration (CIA; Nesbitt and Young 1982) is used in various studies to quantify the degree of weathering. Source area weathering and elemental redistribution during diagenesis can also be assessed using Plagioclase Index of Alteration (PIA; Fedo et al. 1995) and Chemical Index of Weathering (CIW; Harnois 1988).

The CIA, PIA, and CIW values of the Samh shales have been calculated by following the procedure of McLennan (1993), and the results are provided in Table 1. Based on the CIA values, the degree of weathering varies from 73.12 to 81.78 (average = 79.3). The average CIA is within the range of the PAAS values (70–75; Taylor and McLennan 1985). These values indicate a moderate to intense chemical weathering in the source area. A narrow range in CIA values (73–81; Table 1), indicating mature sediments, which are consistent with the  $\text{SiO}_2/\text{Al}_2\text{O}_3$  ratio (Fig. 5). According to the PIA values, the intensity of alteration of source material varies from 85 to 94, with an average of 91. The CIW values suggest the degree of source weathering in the range from 88 to 95, with an average of 93. Average PIA and CIW values (91 and 93 %, respectively) indicate a higher degree of weathering than the values inferred from CIA values (79.3 %).

The CIA values are also plotted in  $\text{Al}_2\text{O}_3 - (\text{CaO}^* + \text{Na}_2\text{O}) - \text{K}_2\text{O}(\text{A}-\text{CN}-\text{K})$  triangular diagram (molecular proportion; Fedo et al. 1996; Fig. 8) which identifies the differentiation of compositional changes associated with chemical weathering and/or source rock composition (Deepthi et al. 2012; Ghosh et al.

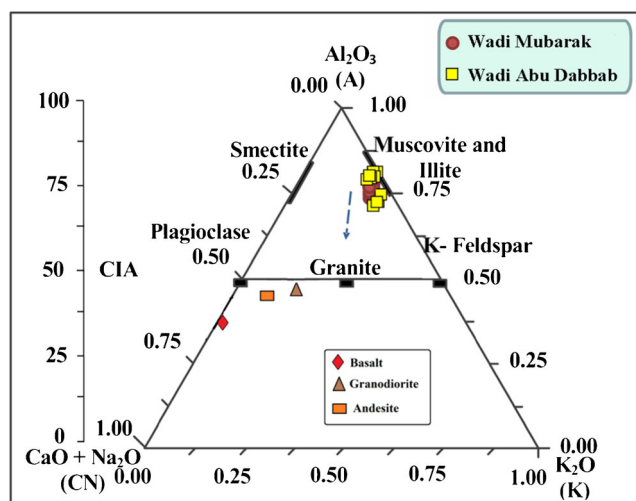


**Fig. 8** A–CN–K ternary diagram of molecular proportions of  $\text{Al}_2\text{O}_3$ – $(\text{CaO} + \text{Na}_2\text{O})$ – $\text{K}_2\text{O}$  (after Nesbitt and Young 1982)

2012). The Samh shales plot above plagioclase–K-feldspar joint and show a narrow linear trend that runs towards the “A” edge (Fig. 8). This is primarily due to removal rates of Na and Ca from plagioclase being generally greater than the removal rates of K from microcline (Nesbitt and Young 1984). The plots trend toward the A apex (Fig. 8) and do not exhibit any inclination toward the K apex indicating that the shales were not subjected to potash metasomatism during diagenesis. When the trend line extended backward, this line intersects the plagioclase–K-feldspar joint near the granite field (probable source rocks). Linear weathering trend of the Samh shales defines a steady-state weathering condition. This is primarily due to removal rate of material is equal to the rate of production of weathering materials (Nesbitt et al. 1997; Nesbitt and Young 2004).

### Provenance

The chemical composition of siliciclastic sediments has been widely used to identify the source rocks characteristics (e.g., Cullers 1995; Armstrong-Altrin et al. 2004, 2012; Zaid 2012, 2015). In order to infer the provenance of siliciclastic rocks, several major- and trace element-based discrimination diagrams have been proposed by various authors (e.g., Roser and Korsch 1988; Floyd et al. 1989; McLennan et al. 1993). On the major element based provenance discrimination diagram of Roser and Korsch (1988), the Samh shales plot in the quartzose sedimentary and felsic igneous provenance fields (Fig. 9).

The silica content of the igneous source rocks can be inferred from the  $\text{Al}_2\text{O}_3/\text{TiO}_2$  ratio of siliciclastic rocks. According to Hayashi et al. (1997), the  $\text{Al}_2\text{O}_3/\text{TiO}_2$  ratio and  $\text{SiO}_2$  contents vary in the igneous rocks as follows: (a) the values of  $\text{Al}_2\text{O}_3/\text{TiO}_2$  were 3 to 8 in mafic igneous rocks ( $\text{SiO}_2$  content from 45 to 52 wt%), (b) the values of  $\text{Al}_2\text{O}_3/\text{TiO}_2$  ratio were 8 to 21 in the intermediate igneous rocks ( $\text{SiO}_2$  content from 53 to 66 wt%), and (c) the values of

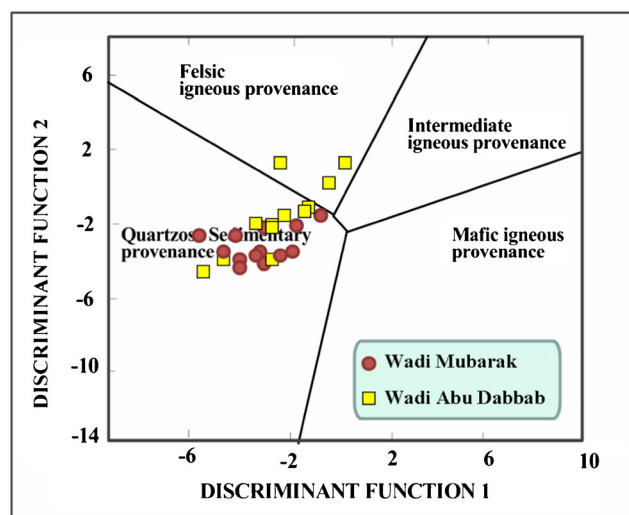


**Fig. 9** Provenance discrimination diagram for shales (after Roser and Korsch 1988). Discriminant function 1 =  $(-1.773 \times \text{TiO}_2\%) + (0.607 \times \text{Al}_2\text{O}_3\%) + (0.76 \times \text{Fe}_2\text{O}_3^{\text{T}}\%) + (-1.5 \times \text{MgO}\%) + (0.616 \times \text{CaO}\%) + (0.509 \times \text{Na}_2\text{O}\%) + (-1.22 \times \text{K}_2\text{O}\%) + (-9.09)$ . Discriminant function 2 =  $(0.445 \times \text{TiO}_2\%) + (0.07 \times \text{Al}_2\text{O}_3\%) + (-0.25 \times \text{Fe}_2\text{O}_3^{\text{T}}\%) + (-1.142 \times \text{MgO}\%) + (0.438 \times \text{CaO}\%) + (0.432 \times \text{Na}_2\text{O}\%) + (1.426 \times \text{K}_2\text{O}\%) + (-6.861)$

$\text{Al}_2\text{O}_3/\text{TiO}_2$  were 21 to 70 in felsic igneous rocks ( $\text{SiO}_2$  content from 66 to 76 wt%). The  $\text{Al}_2\text{O}_3/\text{TiO}_2$  ratio of the Samh shales vary from 10.96 to 22.6 (average = 16.7) and  $\text{SiO}_2$  contents vary from 48.96 to 69.12 wt% (average = 62.1 wt%). These values suggest that the source rocks of the Samh shales are felsic igneous rocks.

On the  $\text{Al}_2\text{O}_3$ – $(\text{CaO} + \text{Na}_2\text{O} + \text{K}_2\text{O})$ – $(\text{FeO}^{\text{T}} + \text{MgO})$  ternary diagram (Hayashi et al. 1997), the shales plot along chlorite–illite trend near smectite field away from  $(\text{FeO}^{\text{T}} + \text{MgO})$  apex and trend toward  $\text{Al}_2\text{O}_3$  apex (Fig. 10a). This diagram reiterates (albeit indirectly) the felsic nature of the source rocks. Concentration of zircon (Zr) is also used for characterizing the nature and composition of source rocks (Hayashi et al. 1997). As the average concentrations of Zr and  $\text{TiO}_2$  do not show a wide variation (Table 2), it may be possible that significant fractionation of Zr and Ti might not have occurred during transportation and deposition of Samh shales. Average Zr content of the Samh shales varies from 135 to 208 ppm (Table 2), which is similar to the average value of granite and granodiorite. The  $\text{TiO}_2$  versus Zr plot (Hayashi et al. 1997) of the Samh shales represents felsic igneous source rocks (Fig. 10b). Overall, the provenance discrimination diagrams indicate that the nature of the source rocks was felsic (granitic).

### Tectonic setting

Several studies have shown that the geochemistry of siliciclastic rocks is significantly controlled by plate tectonic settings of the source area, and consequently sediments

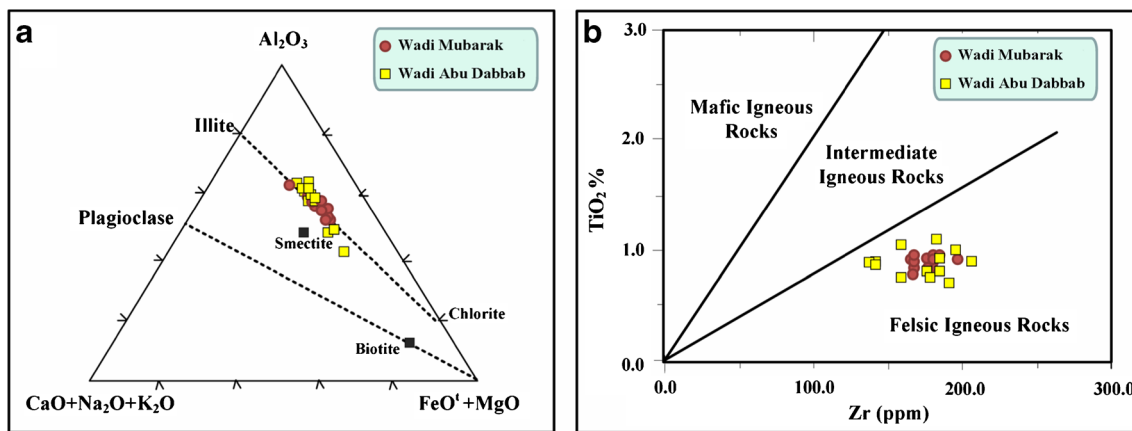


**Fig. 10** Provenance diagrams. **a**  $Al_2O_3$ – $(CaO + Na_2O + K_2O)$ – $(FeO + MgO)$  ternary diagram (after Hayashi et al. 1997). **b**  $TiO_2$  wt% versus Zr (ppm) bivariate diagram (after Hayashi et al. 1997)

derived from different tectonic settings possess specific geochemical signatures (e.g., Bhatia 1983; Bhatia and Crook 1986; Roser and Korsch 1986). Tectonic settings of ancient terrains can be inferred from major- and trace element-based discrimination diagrams (e.g., Bhatia 1983; Bhatia and Crook 1986; Roser and Korsch 1986). These diagrams discriminate oceanic island arc, continental island arc, active continental margin, and passive margin. On the bivariate diagrams of Roser and Korsch (1986) and Bhatia (1983), most shale samples plot in the passive margin field, except few, which fall in the active continental margin field (Fig. 11a, b). This makes it most probable that the Samh shales were deposited chiefly in a passive margin setting. The passive margin comprises rifted continental margins and is developed along the edges of the continents (Bhatia 1983).

However, these diagrams were evaluated by other researchers and they cautioned the use of these previously proposed discrimination diagrams (e.g., Armstrong-Altrin and Verma 2005; Ryan and Williams 2007; Armstrong-Altrin 2015; Armstrong-Altrin et al. 2015b). Recently, Verma and Armstrong-Altrin (2016) proposed two new discriminant function diagrams for the discrimination of active and passive margin settings. On these plots (Fig. 12a, b), the samples exclusively plot in the

passive margin field, which is consistent with bivariate diagrams of Roser and Korsch (1986) and Bhatia (1983) (Fig. 11a, b).

Verma and Armstrong-Altrin (2013) also proposed two discriminant function-based major element diagrams for the tectonic discrimination of siliciclastic sediments from three main tectonic settings: island or continental arc, continental rift, and collision, which have been created for the tectonic discrimination of high-silica [ $(SiO_2)_{adj} = 63–95\%$ ] and low-silica rocks [ $(SiO_2)_{adj} = 35–63\%$ ]. These two new diagrams were constructed based on worldwide examples of Neogene–Quaternary siliciclastic sediments from known tectonic settings,  $\log_e$  ratio transformation of ten major elements with  $SiO_2$  as the common denominator, and linear discriminant analysis of the  $\log_e$ -transformed ratio data. Recently, these diagrams were evaluated by Armstrong-Altrin (2015) and identified a good functioning of these diagrams for discriminating the tectonic setting of older sedimentary basins. Similarly, these diagrams were used in recent studies to discriminate the tectonic setting of a source region, based on sediment geochemistry (Armstrong-Altrin et al. 2014, 2015a, b; Zaid and Gahtani 2015; Zaid 2015). On these plots (high-silica and low-silica diagrams; Fig. 13a, b), the samples exclusively plot in the rift field. The results obtained from

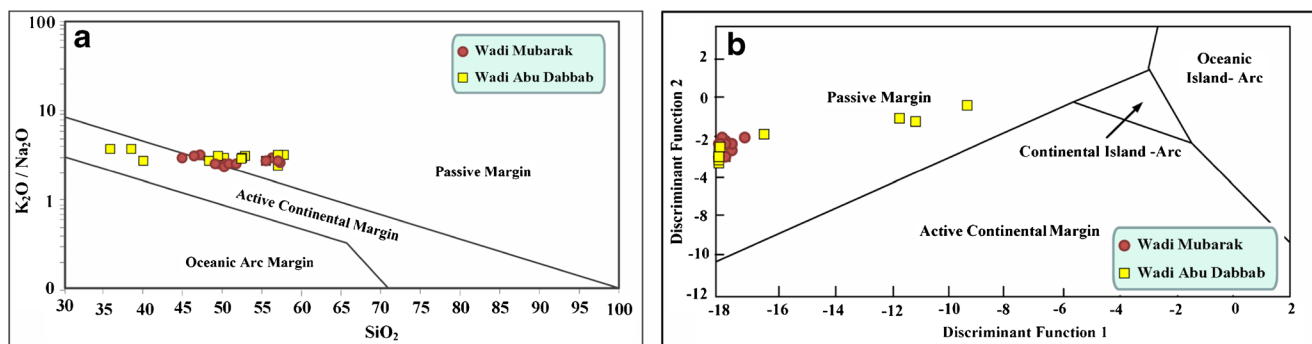


**Fig. 11** Tectonic discrimination diagrams for the Samh shales (fields are demarcated after **a** Roser and Korsch 1986 and **b** Bhatia 1983)

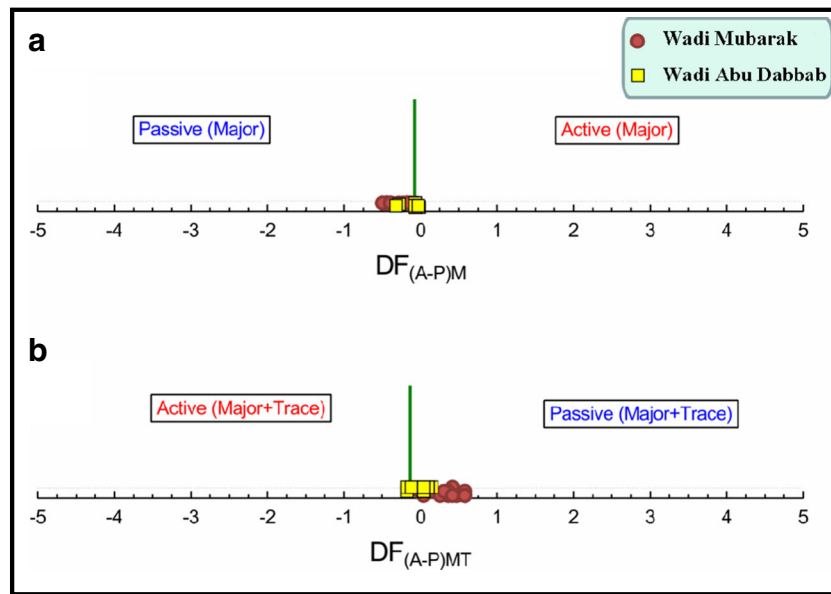


**Fig. 12** The new multidimensional discriminant function diagrams proposed by Verma and Armstrong-Altrin (2016) for the discrimination of active (*A*) and passive (*P*) margin settings. **a** Major element (*M*) based diagram. **b** Combined major and trace element (*MT*)-based diagram. The discriminant function equations are as follows: **a**  $DF_{(A-P)M} = (3.0005 \times ilr1_{Ti}) + (2.8243 \times ilr2_{Al}) + (-1.0596 \times ilr3_{Fe}) + (-0.7056 \times ilr4_{Mn}) + (-0.3044 \times ilr5_{Mg}) + (0.6277 \times ilr6_{Ca}) +$

$(-1.1838 \times ilr7_{Na}) + (1.5915 \times ilr8_{K}) + (0.1526 \times ilr9_{P}) - 5.9948.$  **b**  $DF_{(A-P)MT} = (3.2683 \times ilr1_{Ti}) + (5.3873 \times ilr2_{Al}) + (1.5546 \times ilr3_{Fe}) + (3.2166 \times ilr4_{Mn}) + (4.7542 \times ilr5_{Mg}) + (2.0390 \times ilr6_{Ca}) + (4.0490 \times ilr7_{Na}) + (3.1505 \times ilr8_{K}) + (2.3688 \times ilr9_{P}) + (2.8354 \times ilr10_{Cr}) + (0.9011 \times ilr11_{Nb}) + (1.9128 \times ilr12_{Ni}) + (2.9094 \times ilr13_{V}) + (4.1507 \times ilr14_{Y}) + (3.4871 \times ilr15_{Zr}) - 3.2088$

these two discriminant function-based multi-dimensional diagrams provide a good evidence for the Red Sea–Eastern

Desert tectonic system, which is consistent with the general geology of Egypt (Said 1990).

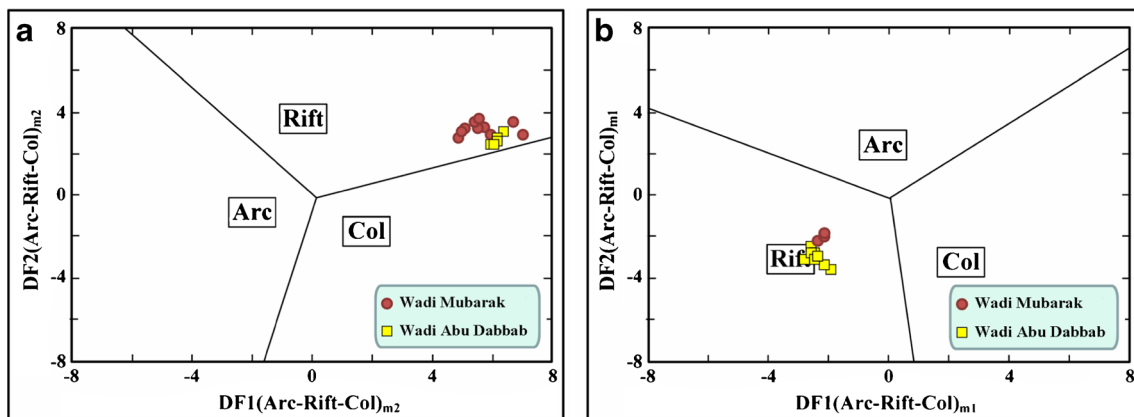


**Fig. 13 a** New discriminant function multi-dimensional diagram proposed by Verma and Armstrong-Altrin (2013) for high-silica clastic sediments from three tectonic settings (arc, continental rift, and collision). The *subscript* m1 in DF1 and DF2 represents the high-silica diagram based on  $\log_e$  ratios of major elements. The discriminant function equations are as follows:  $DF1_{(Arc-Rift-Col)m1} = (-0.263 \times \ln(TiO_2/SiO_2)_{adj}) + (0.604 \times \ln(Al_2O_3/SiO_2)_{adj}) + (-1.725 \times \ln(Fe_2O_3/SiO_2)_{adj}) + (0.660 \times \ln(MnO/SiO_2)_{adj}) + (2.191 \times \ln(MgO/SiO_2)_{adj}) + (0.144 \times \ln(CaO/SiO_2)_{adj}) + (-1.304 \times \ln(Na_2O/SiO_2)_{adj}) + (0.054 \times \ln(K_2O/SiO_2)_{adj}) + (-0.330 \times \ln(P_2O_5/SiO_2)_{adj}) + 1.588.$   $DF2_{(Arc-Rift-Col)m1} = (-1.196 \times \ln(TiO_2/SiO_2)_{adj}) + (1.604 \times \ln(Al_2O_3/SiO_2)_{adj}) + (0.303 \times \ln(Fe_2O_3/SiO_2)_{adj}) + (0.436 \times \ln(MnO/SiO_2)_{adj}) + (0.838 \times \ln(MgO/SiO_2)_{adj}) + (-0.407 \times \ln(CaO/SiO_2)_{adj}) + (1.021 \times \ln(Na_2O/SiO_2)_{adj}) + (-1.706 \times \ln(K_2O/SiO_2)_{adj}) + (-0.126 \times \ln(P_2O_5/SiO_2)_{adj}) - 1.068.$  **b** New discriminant function

multi-dimensional diagram proposed by Verma and Armstrong-Altrin (2013) for low-silica clastic sediments from three tectonic settings (arc, continental rift, and collision). The *subscript* m2 in DF1 and DF2 represents the low-silica diagram based on  $\log_e$  ratio of major elements. Discriminant function equations are as follows:  $DF1_{(Arc-Rift-Col)m2} = (0.608 \times \ln(TiO_2/SiO_2)_{adj}) + (-1.854 \times \ln(Al_2O_3/SiO_2)_{adj}) + (0.299 \times \ln(Fe_2O_3/SiO_2)_{adj}) + (-0.550 \times \ln(MnO/SiO_2)_{adj}) + (0.120 \times \ln(MgO/SiO_2)_{adj}) + (0.194 \times \ln(CaO/SiO_2)_{adj}) + (-1.510 \times \ln(Na_2O/SiO_2)_{adj}) + (1.941 \times \ln(K_2O/SiO_2)_{adj}) + (0.003 \times \ln(P_2O_5/SiO_2)_{adj}) - 0.294.$   $DF2_{(Arc-Rift-Col)m2} = (-0.554 \times \ln(TiO_2/SiO_2)_{adj}) + (-0.995 \times \ln(Al_2O_3/SiO_2)_{adj}) + (1.765 \times \ln(Fe_2O_3/SiO_2)_{adj}) + (-1.391 \times \ln(MnO/SiO_2)_{adj}) + (-1.034 \times \ln(MgO/SiO_2)_{adj}) + (0.225 \times \ln(CaO/SiO_2)_{adj}) + (0.713 \times \ln(Na_2O/SiO_2)_{adj}) + (0.330 \times \ln(K_2O/SiO_2)_{adj}) + (0.637 \times \ln(P_2O_5/SiO_2)_{adj}) - 3.631$



## Conclusions

The Samh Formation consists of sandstone underlies by shale and marl intercalations. The Samh shales are texturally classified as mudstones. Mineralogically, these shales consist mainly of smectite and kaolinite, associated with non clay minerals (abundant quartz and traces of plagioclase, microcline, and halite). Compared to PAAS, the Samh shales are enriched in  $\text{SiO}_2$ ,  $\text{Al}_2\text{O}_3$ , and  $\text{Fe}_2\text{O}_3$  and depleted in  $\text{TiO}_2$ ,  $\text{P}_2\text{O}_5$ , and  $\text{Na}_2\text{O}$  contents and moderately depleted in  $\text{MgO}$  and  $\text{K}_2\text{O}$  contents. Depletion of  $\text{Na}_2\text{O}$  in the shales relative to PAAS suggests either lesser amount of plagioclase detritus in the shales and/or comparatively intense chemical weathering at the source area. Depletion of  $\text{TiO}_2$  and  $\text{K}_2\text{O}$  suggests that phyllosilicate minerals exist in lesser quantities in the shales.

Trace elements like Zr, Cr, Pb, Sc, Rb, and Cs are positively correlated with  $\text{Al}_2\text{O}_3$  indicating that these elements are likely fixed in K-feldspars and clays, while Co, Cd, V, U, Cu, Ni, Th, Ba, Hf, Sr, and Zn show very low or negative correlation with  $\text{Al}_2\text{O}_3$ , indicating that they are not likely bound in the clay minerals.

The CIA, PIA, and CIW values (between 73 and 95) indicate moderate to intense weathering in the source area. The  $\text{SiO}_2$  versus  $(\text{Al}_2\text{O}_3 + \text{K}_2\text{O} + \text{Na}_2\text{O})\%$  diagram indicates that the Samh shales were deposited under arid to semiarid conditions.

The recent tectonic discriminant function diagrams indicate a rift setting for the studied shales. The inferred tectonic setting for the Upper Miocene Samh shales in Marsa Alam is in agreement with the tectonic evolutionary history of the Eastern Desert of Egypt during the Upper Miocene.

**Acknowledgments** The author acknowledges the journal reviewers for their very constructive and helpful comments as well as for editorial comments, which helped to improve the manuscript.

## References

- Ahmed H.A. (1997) Mineralogical and geochemical studies of the black shales intercalated with phosphorite deposits at Abu Tartur area Western Desert, Egypt, M.Sc. thesis, Ain Shams Uni. Cairo, Egypt, 284 p
- Ahmedali S.T. (1989) X-ray fluorescence analysis in the geological sciences. *Advances in Methodology*, Vol. 7. Geological Association of Canada, short course, 308 p
- Akarish AIM, El-Gohary AM (2008) Petrography and geochemistry of lower Paleozoic sandstones, East Sinai, Egypt: implications for provenance and tectonic setting. *J Afr Earth Sci* 52:43–54
- Armstrong-Altrin JS (2009) Provenance of sands from Cazonas, Acapulco, and Bahía Kino beaches, Mexico. *Revista Mexicana de Ciencias Geológicas* 26(3):764–782
- Armstrong-Altrin JS (2015) Evaluation of two multidimensional discrimination diagrams from beach and deep-sea sediments from the Gulf of Mexico and their application to Precambrian clastic sedimentary rocks. *Int Geol Rev* 57:1444–1459
- Armstrong-Altrin JS, Verma SP (2005) Critical evaluation of six tectonic setting discrimination diagrams using geochemical data of Neogene sediments from known tectonic setting. *Sediment Geol* 177:115–129
- Armstrong-Altrin JS, Lee YI, Verma SP, Ramasamy S (2004) Geochemistry of sandstones from the Upper Miocene Kudankulam Formation, southern India: implications for provenance, weathering, and tectonic setting. *J Sediment Res* 74:285–297
- Armstrong-Altrin JS, Lee YI, Kasper-Zubillaga JJ, Carranza-Edwards A, Garcia D, Eby N, Balaran V, Cruz-Ortiz NL (2012) Geochemistry of beach sands along the western Gulf of Mexico, Mexico: implication for provenance. *Chem Erde/Geochem* 72:345–362
- Armstrong-Altrin JS, Nagarajan R, Lee YI, Kasper-Zubillaga JJ, Córdoba-Saldaña LP (2014) Geochemistry of sands along the San Nicolás and San Carlos beaches, Gulf of California, Mexico: implication for provenance. *Turk J Earth Sci* 23:533–558
- Armstrong-Altrin JS, Machain-Castillo ML, Rosales-Hoz L, Carranza-Edwards A, Sanchez-Cabeza JA, Ruíz-Fernández AC (2015a) Geochemistry of deep sea sediments from the south-western Gulf of Mexico, Mexico: implication for depositional environment. *Cont Shelf Res*. doi:10.1016/j.csr.2015.01.003
- Armstrong-Altrin JS, Nagarajan R, Balaran V, Natalhy-Pineda O (2015b) Petrography and geochemistry of sands from the Chachalacas and Veracruz beach areas, western Gulf of Mexico, Mexico: constraints on provenance and tectonic setting. *J South Am Earth Sci* 64:199–216
- Bhatia MR (1983) Plate tectonics and geochemical composition of sandstones. *J Geol* 91:611–627
- Bhatia MR, Crook KAW (1986) Trace element characteristics of graywackes and tectonic setting discrimination of sedimentary basins. *Contrib Mineral Petrol* 92:181–193
- Chamley H (1989) *Clay sedimentology*. Springer, Berlin, p. 623
- Condie KC (1993) Chemical composition and evolution of the upper continental crust: contrasting results from surface samples and shales. *Chem Geol* 104:1–37
- Condie KC, Boryta MD, Liu J, Quian X (1992) The origin of khondalites: geochemical evidence from the Archean to Early Proterozoic granulite belt in the North China craton. *Precam Res* 59:207–223
- Cox R, Lower DR, Cullers RL (1995) The influence of sediment recycling and basement composition on evolution of mudrock chemistry in the southwestern United States. *Geochim Cosmochim Acta* 59:2919–2940
- Cullers RL (1995) The controls on the major- and trace-element evolution of shales, siltstones and sandstones of Ordovician to Tertiary age in the Wet Mountains region, Colorado, U.S.A. *Chem. Geol* 123:107–131
- Davis JC (1986) *Statistics and data analysis in geology*. Wiley, 646 pp
- Deepthi K, Natesan U, Muthulakshmi AL, Ferrer VA, Venugopalan VP, Narasimhan SV (2012) Geochemical characteristics and depositional environment of Kalpakkam, Southeast coast of India. *Environ Earth Sci*
- El-Akkad S, Dardir AA (1966) Geology of the Red Sea Coast between Ras Shagra and Mersa Alam with short notes on results of exploratory work at Gabal El-Rusas lead-zinc deposits. *Geologic Survey of Egypt, Paper* 35:1–67
- Fedo CM, Nesbitt HW, Young GM (1995) Unraveling the effects of K metasomatism in sedimentary rocks and paleosols with implications for palaeoweathering conditions and provenance. *Geology* 23:921–924
- Fedo CM, Eriksson KA, Krogstad EJ (1996) Geochemistry of shales from the Archean (3.0 Ga) Buhwa Greenstone Belt, Zimbabwe: implications for provenance and source-area weathering. *Geochim Cosmochim Acta* 60:1751–1763
- Floyd PA, Franke W, Shail R, Dorr W (1989) Geochemistry and tectonic setting of Lewisian clastic metasediments from the Early Proterozoic Loch Maree Group of Gairloch, NW Scotland. *Precam Res* 45:203–214
- Fyffe LR, Pickerill RK (1993) Geochemistry of Upper Cambrian-Lower Ordovician black shale along a northeastern Appalachian transect. *Geol Soc Am Bull* 105:896–910

- Ghandour IM, Harue M, Wataru M (2003) Mineralogical and chemical characteristics of Bajocian-Bathonian shales, G. Al-Maghara, North Sinai, Egypt: climatic and environmental significance. *Geochem J* 37:87–108
- Ghosh S, Sarkar S, Ghosh P (2012) Petrography and major element geochemistry of the Permo-Triassic sandstones, central India: implications for provenance in an intracratonic pull-apart basin. *J Asian Earth Sci* 43:207–240
- Gindy AR (1983) Factors controlling the clay mineralogy of Egyptian Phanerozoic mudrocks and marls. *Geol Jb, B* 49:3–25 Hannover
- Gromet LP, Dymek RF, Haskin LA, Korotev RL (1984) The North American shale composite : its compilations, major and trace element characteristics. *Geochim Cosmochim Acta* 48:2469–2482
- Hardy R, Tucker M (1988) X-ray powder diffraction of sediments. In: Tucker M (ed) *Techniques in Sedimentology*. Blackwell Science, Cambridge, pp. 191–228
- Harnois L (1988) The CIW index: a new chemical index of weathering. *Sed Geol* 55:319–322
- Hayashi KI, Fujisawa H, Holland HD, Ohmoto H (1997) Geochemistry of ~1.9 Ga sedimentary rocks from northern Labrador, Canada. *Geochim Cosmochim Acta* 61(19):4115–4137
- Hendriks F, Luger P, Strouhal A (1990) Early tertiary marine palygorskite and sepiolite neof ormation in SE Egypt. *Z Dt Geol Ges* 141:87–97
- Herron MM (1988) Geochemical classification of terrigenous sands and shales from core or log data. *J Sediment Petrol* 58:820–829
- Ismael SI (1996) Mineralogical and geochemical studies of the black shales intercalated with the phosphate deposits along the Red Sea coast, Egypt. Ph.D. Thesis. Ain Shams Uni. Cairo, Egypt
- Issawi B, Francis MH, Youssef EAA, Osman RA (2009) *The Phanerozoic geology of Egypt, a geodynamic approach*, (2nd ed.). Egypt Miner Res Authority Spec Publ No 81:589
- Knauer GA, Martin JH (1973) Seasonal variation of Cd, Co, Mn, Pb, and Zn in water and phytoplankton in Monterey bay, California. *Limnol. Oceanogr.* Milwaukee 18:597–604
- Kora M, Abdel-Fattah Z (2000) Pliocene and Plio-Pleistocene macrofauna from the Red Sea coastal plain (Egypt): biostratigraphy and biogeography. *Geol Palaeontol* 34:219–235
- Lee YI (2009) Geochemistry of shales of the Upper Cretaceous Hayang Group, SE Korea: implications for provenance and source weathering at an active continental margin. *Sed Geol* 215:1–12
- McLennan SM (1993) Weathering and global denudation. *J Geol* 101: 295–303
- McLennan SM, Taylor SR, Eriksson KA (1983) Geochemistry of Archaean shales from the Pilbara Supergroup, Western Australia. *Geoch et Cosmoch Acta* 47(7):1211–1222
- McLennan SM, Hemming S, Mcdaniel DK, Hanson GN (1993) Geochemical approaches to sedimentation, provenance and tectonics. In: Johnsson, J.M., Basu, A. (eds.), *Processes controlling the composition of clastic sediments*. Geological Society of America, Special Paper 284: 21–40
- Millot G (1970) *Geology of clays*. Springer, Heidelberg—New York 429 p
- Mondal MEA, Wani H, Mondal B (2012) Geochemical signature of provenance, tectonics and chemical weathering in the Quaternary flood plain sediments of the Hindon River, Gangetic plain, India. *Tectonophysics* 566–7:87–94
- Moore DM, Reynolds RC Jr (1997) *X-ray diffraction and the identification and analysis of clay minerals*. Oxford University Press, New York, p. 378
- Moosavirad SM, Janardhana MR, Sethumadhav MS, Moghadam MR, Shankara M (2011) Geochemistry of lower Jurassic shales of the Shemshak Formation, Kerman Province, Central Iran: provenance, source weathering and tectonic setting. *Chem Erde* 71:279–288
- Moosavirad SM, Janardhana MR, Sethumadhav MS, Narasimha KNP (2012) Geochemistry of Lower Jurassic sandstones of Shemshak Formation, Kerman Basin, Central Iran: provenance, source weathering and tectonic setting. *J Geol Soc India* 79:483–496
- Nagarajan R, Madhavaraju J, Nagendra R, Armstrong-Altrin JS, Moutte J (2007) Geochemistry of Neoproterozoic shales of the Rabanpalli formation, Bhima Basin, northern Karnataka, southern India: implications for provenance and paleoredox conditions. *Revista Mexicana de Ciencias Geológicas* 24(2):150–160
- Nath NB, Kunzendorf H, Pluger WL (2000) Influence of provenance and sedimentary processes on the elemental ratios of the fine-grained fraction of the bedload sediments from the Vembanad Lake and the adjoining continental shelf, south-coast of India. *J Sed Res* 70: 1081–1094
- Nesbitt HW, Young GM (1982) Early Proterozoic climates and plate motions inferred from major element chemistry of lutites. *Nature* 299:715–717
- Nesbitt HW, Young GM (1984) Prediction of some weathering trends of plutonic and volcanic rocks based on thermodynamic and kinetic considerations. *Geochim Cosmochim Acta* 48:1523–1534
- Nesbitt HW, Young GM (2004) Ancient climatic and tectonic settings inferred from paleosols developed on igneous rocks. In: Eriksson PG, Alternan W, Nelson DR, Mueller WU, Catuneanu O (eds) *The Precambrian Earth: tempos and events*. Elsevier, Amsterdam, pp. 482–493
- Nesbitt HW, Fedo CM, Young GM (1997) Quartz and feldspar stability, steady and non-steady-state weathering, and petrogenesis of siliciclastic sands and muds. *J Geol* 105:173–191
- Purser, B., Philobos, E. (1993) The sedimentary expressions of rifting in the NW Red Sea, Egypt. Geological Society of Egypt, Special Publication 1: 1–46.
- Roser BP, Korsch RJ (1986) Determination of tectonic setting of sandstone-mudstone suites using SiO<sub>2</sub> content and K<sub>2</sub>O/Na<sub>2</sub>O ratio. *J Geol* 94(5):635–650
- Roser BP, Korsch RJ (1988) Provenance signatures of sandstone-mudstone suites determined using discriminant function analysis of major-element data. *Chem Geol* 67:119–139
- Ryan KM, Williams DM (2007) Testing the reliability of discrimination diagrams for determining the tectonic depositional environment of ancient sedimentary basins. *Chem Geol* 242:103–125
- Said R (1990) *The geology of Egypt*. A.A. Balkema, Rotterdam, Netherlands, p. 734
- Spalletti LA, Limarino CO, Pinol FC (2012) Petrology and geochemistry of Carboniferous siliciclastics from the Argentine Frontal Cordillera: a test of methods for interpreting provenance and tectonic setting. *J S Am Earth Sci* 36:32–54
- Taylor SR, McLennan SM (1985) *The continental crust: its composition and evolution*. Blackwell, Oxford, 312
- Turekian KK, Wedepohl KH (1961) Distribution of the elements in some major units of the Earth's crust. *Bull Geol Soc Am* 72:175–192
- Verma SP, Armstrong-Altrin JS (2013) New multi-dimensional diagrams for tectonic discrimination of siliciclastic sediments and their application to Precambrian basins. *Chem Geol* 355:117–180
- Verma SP, Armstrong-Altrin JS (2016) Geochemical discrimination of siliciclastic sediments from active and passive margin settings. *Sediment Geol* 332:1–12
- Vine JD, Tourtelot EB (1970) Geochemistry of black shales a summary report. *Econ Geol* 65:253–273
- Zaid SM (2002) Geo-environmental study of north Marsa Alam, Red Sea, Egypt. M. Sc. Thesis. Zagazig Univ., Egypt, p. 280
- Zaid SM (2012) Provenance, diagenesis, tectonic setting and geochemistry of Rudies sandstone (Lower Miocene), Warda Field, Gulf of Suez. *Egypt J Afr Earth Sci* 66–7:56–71
- Zaid SM (2013) Provenance, diagenesis, tectonic setting and reservoir quality of the sandstones of the Kareem Formation, Gulf of Suez, Egypt. *J Afr Earth Sci* 85:31–52

Zaid SM (2015) Geochemistry of sandstones from the Pliocene Gabir Formation, north Marsa Alam, Red Sea, Egypt: implication for provenance, weathering and tectonic setting. *J Afr Earth Sci* 102:1–17

Zaid SM, Gahtani FA (2015) Provenance, diagenesis, tectonic setting and geochemistry of Hawkesbury sandstone (Middle Triassic), southern Sydney Basin, Australia. *Turk J Earth Sci* (in press).